Beyond Yolk–Shell Nanoparticles: Fe_3O_4@Fe_3C Core@Shell Nanoparticles as Yolks and Carbon Nanospindles as Shells for Efficient Lithium Ion Storage

Jianan Zhang,[†] Kaixi Wang,[†] Qun Xu,[*,†] Yunchun Zhou,[§] Fangyi Cheng,[∥] and Shaojun Guo[*,‡]

[†]College of Materials Science and Engineering, Zhengzhou University, Zhengzhou 450052, People's Republic of China, [‡]Physical Chemistry and Applied Spectroscopy, Los Alamos National Laboratory, Los Alamos, New Mexico 87545, United States, [§]National Analytical Research Center of Electrochemistry and Spectroscopy, Changchun Institute of Applied Chemistry, Chinese Academy of Sciences, Changchun 130022, People's Republic of China, and [∥]Key Laboratory of Advanced Energy Materials Chemistry (Ministry of Education), Nankai University, Tianjin 300071, People's Republic of China

ABSTRACT To well address the problems of large volume change and dissolution of Fe_3O_4 nanomaterials during Li^+ intercalation/extraction, herein we demonstrate a one-step *in situ* nanospace-confined pyrolysis strategy for robust yolk–shell nanospindles with very sufficient internal void space (VSIVS) for high-rate and long-term lithium ion batteries (LIBs), in which an Fe_3O_4@Fe_3C core@shell nanoparticle is well confined in the compartment of a hollow carbon nanospindle. This particular structure can not only introduce VSIVS to accommodate volume change of Fe_3O_4 but also afford a dual shell of Fe_3C and carbon to restrict Fe_3O_4 dissolution, thus providing dual roles for greatly improving the capacity retention. As a consequence, Fe_3O_4@Fe_3C–C yolk–shell nanospindles deliver a high reversible capacity of 1128.3 mAh g^{-1} at even 500 mA g^{-1}, excellent high rate capacity (604.8 mAh g^{-1} at 2000 mA g^{-1}), and prolonged cycling life (maintaining 1120.2 mAh g^{-1} at 500 mA g^{-1} for 100 cycles) for LIBs, which are much better than those of Fe_3O_4@C core@shell nanospindles and Fe_3O_4 nanoparticles. The present Fe_3O_4@Fe_3C–C yolk–shell nanospindles are the most efficient Fe_3O_4-based anode materials ever reported for LIBs.

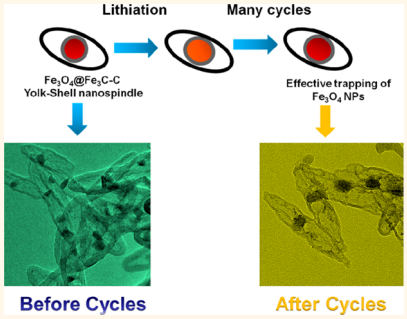

KEYWORDS: yolk–shell structure · iron oxide · iron carbonide · core–shell structure · lithium ion battery

Owing to their high theoretical capacity (*ca.* 924 mAh g^{-1}),[1−5] no toxicity, and low cost, great efforts have been devoted to develop advanced Fe_3O_4-based nanomaterials for their use as advanced anode materials for lithium ion batteries (LIBs).[6−12] Unfortunately, almost all the existing Fe_3O_4 nanomaterials for LIBs suffer from large irreversible capacity loss, low initial Coulombic efficiency, and poor rate capability and cycling stability due to their intrinsically low conductivity, large volume change, and rapid dissolution/aggregation during the repeated lithiation/dethiation process (Scheme 1a). To circumvent these obstacles, recent significant advances have moved to engineer new Fe_3O_4-based nanomaterials with a special design for enhancing LIBs. Typical examples include the synthesis of Fe_3O_4–carbon yolk–shell nanoparticles (NPs) with a small internal void space using a complex multistep template-assisted strategy,[13,14] the preparation of Fe_3O_4 NPs embedded in carbon foam using an expensive atomic layer deposition method,[7] and the design of Fe_3O_4 NPs encapsulated onto two-dimensional (2D) porous carbon through a wet chemical deposition or *in situ* formation strategy,[4,15] Even though these strategies can facilitate strain relaxation and electron transport with suppressed mechanical fracture for a partly improved capacity and stability for LIBs, inevitably these specially designed Fe_3O_4-based nanomaterials suffer from both the fracture of Fe_3O_4 and carbon shell and also the dissolution of Fe_3O_4 due to no or insufficient internal void space by reduplicative volume

* Address correspondence to qunxu@zzu.edu.cn (Q. Xu); sguo@lanl.gov or shaojun.guo.nano@gmail.com (S. Guo).

Received for review February 3, 2015 and accepted February 25, 2015.

Published online February 25, 2015
10.1021/acsnano.5b00760

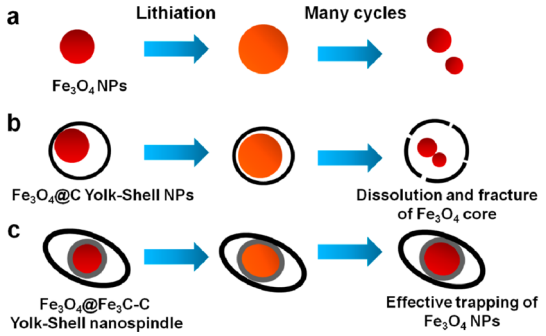

Scheme 1. Schematic illustration of morphological and volumetric changes during electrochemical cycling. (a) Fe_3O_4 NPs (large volume expansion, cracking, and dissolution during lithiation), (b) Fe_3O_4–C yolk–shell NPs (partial volumetric expansion, fracture, and dissolution in nanovoid space), and (c) Fe_3O_4@Fe_3C–C yolk–shell nanospindles with very sufficient internal void space (Fe_3O_4@Fe_3C core@shell NPs persist during lithiation, leading to excellent capacity retention).

variation (Scheme 1b).[3] That means that the introduction of only a small internal void in these Fe_3O_4/carbon materials is still not good enough (not ideal) to solve the significant stability and capacity issues of LIBs.

Recently, iron carbide (Fe_3C) materials have become of great interest in renewable energy conversion and storage due to their thermal stability, high resistance against oxidation, excellent mechanical strength, and catalytic activity.[16−18] They have shown obvious advantages as shell materials by improving the capacity retention during LIB cycles[17−19] and also possessing catalytic activity and stability for oxygen reduction reactions.[20,21] In this regard, the remarkable characteristics of a yolk–shell structure and Fe_3C materials motivated us to find out whether we can rationally design a new class of Fe_3C/C-based nanomaterials with sufficient internal void space as highly efficient anode materials for high-rate and long-term LIBs.

Herein, we report a one-step new nanospace pyrolysis strategy for the *in situ* synthesis of unexpected yet very useful Fe_3O_4@Fe_3C core@shell NPs–carbon yolk–shell nanospindles with very large internal void space (denoted as Fe_3O_4@Fe_3C–C yolk–shell nanospindles) for developing high-performance LIBs with high capacity, rate capability, and cycle stability (Scheme 1c). In the Fe_3O_4@Fe_3C–C yolk–shell nanospindles, an Fe_3O_4@Fe_3C core@shell NP with a diameter of 15–20 nm was well confined in the compartment of hollow carbon nanospindles with a wall thickness of 3–5 nm, and the internal void volume ratio can reach about 75%. We found that such Fe_3O_4@Fe_3C–C yolk–shell nanospindles can well address several important challenging issues related to LIBs: (a) The much larger internal void space provided by Fe_3O_4@Fe_3C–C yolk–shell nanospindles than those of the reported Fe_3O_4–C yolk–shell NPs with small internal void space and Fe_3O_4 NPs can accommodate the larger space for allowing the large volumetric expansion of Fe_3O_4 during lithiation,

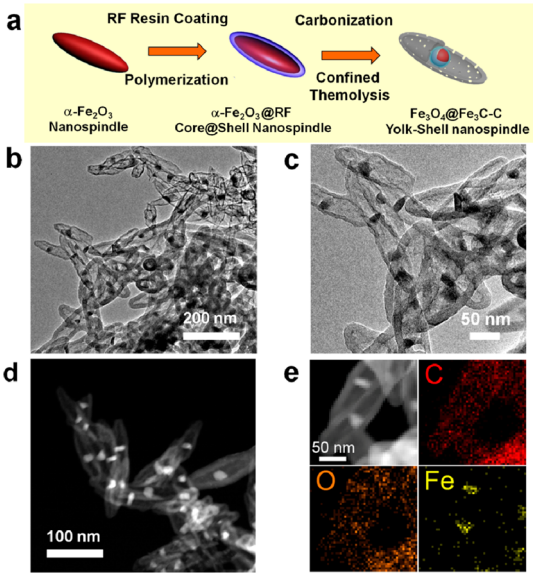

Figure 1. (a) Schematic illustration of the synthesis of the Fe_3O_4@Fe_3C–C yolk–shell nanospindles. (b, c) TEM image, (d) STEM image, and (e) TEM-EDS mapping of Fe_3O_4@Fe_3C–C yolk–shell nanospindles.

thus preserving the structural integrity. (b) Fe_3C as a shell material can act as an armor or buffer for protecting the Fe_3O_4 core from dissolution after the long-term cycling. (c) The porous carbon shells with high electron conductivity from the yolk–shell nanospindles have multimodel pores, providing perfect 3D pathways for lithium ion transport. As a consequence, our new Fe_3O_4@Fe_3C–C yolk–shell nanospindles deliver a high reversible capacity of 1128.3 mAh g^{-1} at even 500 mA g^{-1}, excellent high rate capacity (604.8 mAh g^{-1} at 2000 mA g^{-1}), and prolonged cycling life (maintaining 1120.2 mAh g^{-1} at 500 mA g^{-1} for 100 cycles) for lithium ion storage. To the best of our knowledge, the present Fe_3O_4@Fe_3C–C yolk–shell nanospindles are the most efficient Fe_3O_4-based anode materials ever reported for LIBs.

RESULTS AND DISCUSSION

The Fe_3O_4@Fe_3C–C yolk–shell nanospindles were synthesized through a one-step *in situ* nanospace-confined pyrolysis of as-prepared Fe_2O_3@resorcinol-formaldehyde (RF) core@shell nanospindles (see details in the Experimental Section). Figure 1a illustrates the synthetic protocol of the Fe_3O_4@Fe_3C–C yolk–shell nanospindles. First, the uniform α-Fe_2O_3 nanospindles 30 nm in width and 100 nm in length were prepared through a hydrothermal reaction of ferric chloride (Figure S1a–c).[22−24] Then, the as-prepared α-Fe_2O_3 nanospindles were directly coated with a conformal RF resin layer in an ethanol–ammonia–water system, resulting in the formation of an α-Fe_2O_3@RF core–shell structure. Figure S1d–f show the scanning electron microscope (SEM) and transmission electron microscopy (TEM) images of α-Fe_2O_3@RF core@shell

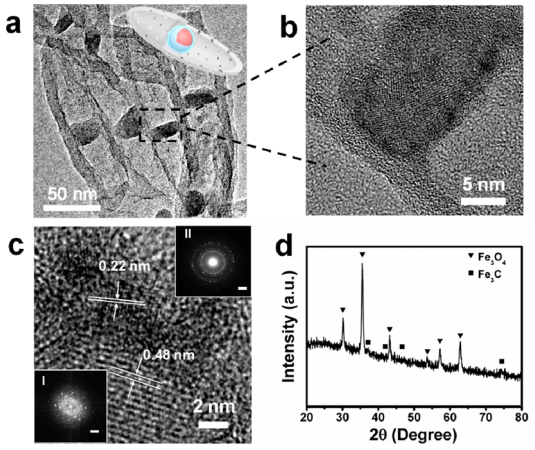

Figure 2. (a, b) TEM and (c) HRTEM images of Fe_3O_4@Fe_3C−C yolk−shell nanospindles (the inset shows the corresponding FFT image of Fe_3O_4 (I) and Fe_3C (II) with scale bars being 5 nm^{-1}). (d) XRD patterns of Fe_3O_4@Fe_3C−C yolk−shell nanospindles.

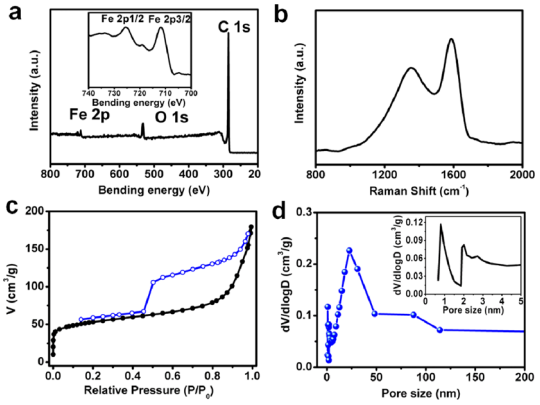

Figure 3. (a) XPS, (b) Raman spectra, (c) N_2 adsorption and desorption isotherms, and (d) pore size distribution of Fe_3O_4@Fe_3C−C yolk−shell nanospindles.

structures. It is found that all α-Fe_2O_3 nanospindles are wrapped by RF resins with a shell thickness of 5−8 nm. These α-Fe_2O_3 nanospindles can be reduced by RF resins at high temperature, and 550 °C annealing treatment in a N_2 atmosphere allows the partial "escape" of the core from the carbon shell, resulting in an individual Fe_3O_4@Fe_3C core@shell NP confined in a large carbon nanospindle with a large internal void space (Figure 1b,c). The redundant Fe-related materials aggregate into large particles and can be easily removed by precipitation and filtration. Figure 1d shows the scanning TEM (STEM) image of the Fe_3O_4@Fe_3C−C yolk−shell nanospindles. An Fe_3O_4@Fe_3C core@shell NP is well-encapsulated in the interior of the compartment for each carbon nanospindle. This interesting structure is further confirmed by detecting the elemental distribution by the STEM-energy-dispersed spectroscopy (EDS) mapping technique, as shown in Figure 1e. Within the yolk−shell nanospindles, Fe distributes intermittently and the C element uniformly distributes on the overall nanospindle, further supporting the formation of Fe_3O_4@Fe_3C−C yolk−shell nanospindles.

More detailed structural analysis of Fe_3O_4@Fe_3C−C yolk−shell nanospindles was further examined by high-magnification TEM and high-resolution TEM (HRTEM) and X-ray diffraction (XRD). Figure 2a,b show the typical high-magnification TEM image of an Fe_3O_4@Fe_3C−C yolk−shell nanospindle. It is found that a small NP with a diameter of 15−20 nm is sandwiched between the carbon shells, resulting in a large void space of about 75% within the nanospindle (Figure 2a). A larger magnified TEM image of an individual nanospindle (Figure 2b) reveals that the carbon layer with numerous microspores has a thickness of only 3−5 nm. Also the confined NP displays a core@shell structure, evidenced by the dark sheath around the light central nanocrystal. More direct evidence for the Fe_3O_4@Fe_3C core@shell structure is from an HRTEM image (Figure 2c), showing the well-identified Fe_3O_4 (111) lattice fringes with a *d*-spacing of 0.48 nm (the central part) and Fe_3C (211) lattice fringes of 0.22 nm (dark shell part).[17,18,21] Furthermore, the corresponding fast Fourier transformation (FFT) images (inset of Figure 2c) show that insets I and II are assigned to the cubic structure of the Fe_3O_4 crystal core and Fe_3C crystalline shell, respectively. In addition, the XRD pattern of the Fe_3O_4@Fe_3C−C yolk−shell nanospindles (Figure 2d) exhibits both the typical (220), (311), and (400) peaks indexed to Fe_3O_4 (JCPD No 65-3107)[25,26] and the weak (210), (211), and (112) peaks indexed to Fe_3C (JCPDS No. 89-2867).[27,28] No additional peaks are observed, indicating the total conversion of Fe_2O_3 to Fe_3O_4@Fe_3C core@shell NPs during the carbonization.

Figure 3a shows the X-ray photoelectron spectroscopy (XPS) spectrum of Fe_3O_4@Fe_3C−C yolk−shell nanospindles, showing the existence of C, Fe, and O elements. The high-resolution XPS spectrum (inset of Figure 3a) for the Fe 2p is a typical core-level spectrum of Fe_3O_4 with broad peaks around 710.8 and 724.2 eV that correspond to Fe 2P3/2 and Fe 2P1/2 states, respectively.[15,29] The Raman spectrum was further used to evaluate the graphitic quality of the carbon shell in Fe_3O_4@Fe_3C−C yolk−shell nanospindles (Figure 3b). A small intensity ratio of I_D/I_G (0.81), even lower than that of graphene, suggests a high crystalline degree of carbon in Fe_3O_4@Fe_3C−C yolk−shell nanospindles.[30−32] This is beneficial to improve the electrical conductivity of Fe_3O_4@Fe_3C−C yolk−shell nanospindles. The thermogravimetric analysis (TGA) of Fe_3O_4@Fe_3C−C yolk−shell nanospindles, carried out in air at a heating rate of 5 °C/min, was used to determine the mass percentage of Fe_3O_4@Fe_3C core@shell NPs, showing the remaining mass percentage of Fe_2O_3 is about 68.2% (Figure S2). Considering the amount of Fe_3C is small, the carbon amount of Fe_3O_4@Fe_3C−C yolk−shell nanospindles can be determined to be ~34.1%. The porous characteristic of Fe_3O_4@Fe_3C−C yolk−shell

nanospindles was determined by N_2 sorption analysis. As shown in Figure 3c, the N_2 sorption isotherms of Fe_3O_4@Fe_3C−C yolk−shell nanospindles show the type I with a well-defined knee at low P/P_0 (0.0−0.1), implying the existence of a microspore in the carbon shell, while the isotherm changes to type IV at P/P_0 = 0.45−1, mainly attributed to the inner void channel.[33,34] The Brunauer−Emmett−Teller (BET) surface area and the total pore volume of Fe_3O_4@Fe_3C−C yolk−shell nanospindles are measured to be 183.9 m^2/g and 0.23 cm^3/g, respectively, which are higher than those of previously reported Fe_3O_4-based hybrid materials (see Table S1, Supporting Information). The pore size distribution (PSD) for adsorption data, based on the Barrett−Joyner−Halenda (BJH) method, is given in Figure 3d. The Fe_3O_4@Fe_3C−C yolk−shell nanospindles show a hierarchical pore size distribution of 0.8, 2.2, and 2.7 nm (inset of Figure 3d) with a big cavity (~22.8 nm) from the void space and better pore structure compared to the previous Fe_3O_4−C composite nanomaterials (Table S1). Such a multimodel porous structure will be significant for the rapid mass diffusion of electrolyte and the accommodation of volume change of Fe_3O_4 NPs, thus leading to a high capacity and excellent cycling stability.

The temperature-dependent structure change of Fe_3O_4@Fe_3C−C yolk−shell nanospindles under high-temperature annealing conditions in N_2 was used to study the formation mechanism of Fe_3O_4@Fe_3C−C yolk−shell nanospindles. When the annealing temperature is lowered to 450 °C, the α-Fe_2O_3 cores broke into smaller NPs (Figure S3a) and were simultaneously reduced by a carbon precursor and finally converted to metallic Fe phase, confirmed by XRD analysis (Figure S4). When the annealing temperature went up to 550 °C, Fe_3O_4@Fe_3C−C yolk−shell nanospindles were obtained. This is because the nanoscaled metallic iron fused and flowed out from the porous carbon shell, verified by the bulk Fe-based materials outside the nanospindles, as seen in Figure S3b. With the increase of annealing temperature to 650 °C (Figure S3c), partial Fe_3O_4 was further transformed to Fe phase (detected by the XRD pattern in Figure S4), and a higher temperature (750 °C) could lead to only the empty carbon shell (Figure S3d).

In order to better understand the role of the RF shell in forming the particular yolk−shell nanospindles, the RF resin shell was changed to amorphous carbon by polymerizing glucose using the hydrothermal carbonization method. For the parallel comparison, the as-prepared Fe_3O_4@polymerizd glucose core@shell nanospindles were also annealed at 550 °C under a N_2 atmosphere (see details in the Experimental Section). The results from the TEM images and XRD before (Figure S5a,b,e) and after annealing (Figure S5c, d,f) reveal that although the iron oxide crystal phase transformed from Fe_2O_3 to Fe_3O_4 under the same

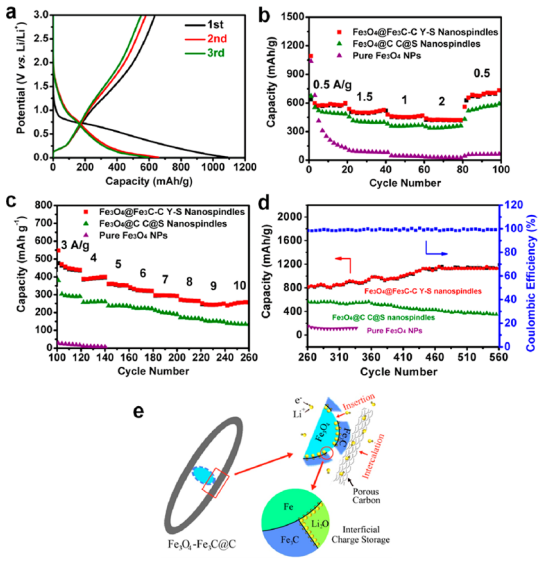

Figure 4. (a) Galvanostatic charge/discharge profiles of Fe_3O_4@Fe_3C−C yolk−shell nanospindles at a current density of 500 mA g^{-1} for the first three cycles. (b, c) Capacity retention of Fe_3O_4@Fe_3C−C yolk−shell nanospindles, Fe_3O_4@C core@shell nanospindles, and pure Fe_3O_4 NPs from (c) 500 to 2000 mA/g and (d) from 3000 to 10 000 mA/g. (d) Subsequent cycling tests of Fe_3O_4@Fe_3C−C yolk−shell nanospindles (red and black marks represent charge and discharge capacities, respectively), Fe_3O_4@C core@shell nanospindles, and pure Fe_3O_4 NPs at 500 mA/g from the 261st to the 560th cycle. (e) Proposed lithium storage by intercalation into the carbon pores and insertion into the lattice of the active material, followed by additional charge separation at the two-phase boundaries to form space charge layers.

carbonization treatment, only Fe_3O_4@C core@shell nanospindles could be obtained. In this regard, we compared the BET surface area, pore size distribution, and pore volume of the Fe_3O_4@Fe_3C−C yolk−shell and Fe_3O_4@C core@shell nanospindles (Figure S6). The former shows a larger pore size and volume than the latter. This will cause the carbon shell from the Fe_3O_4@Fe_3C−C yolk−shell nanospindles to provide a better route for the Fe to get out and further form Fe-based materials at high temperature. Therefore, all these control experiments reveal that the larger pore provided by Fe_3O_4@Fe_3C−C yolk−shell nanospindles during the high-temperature annealing treatment may play the key role in the formation of our particular yolk−shell structure.

The electrochemical performance of the Fe_3O_4@-Fe_3C−C yolk−shell nanospindles, Fe_3O_4@C core@shell nanospindles, and pure Fe_3O_4 NPs[35,36] was investigated by assembling them into coin-type 2032 cells with lithium foil as the reference electrode. Figure 4a shows the charge/discharge profiles of Fe_3O_4@Fe_3C−C yolk−shell nanospindles at the first three cycles from 3 to 0.005 V at 500 mA/g. The first discharge curve presents a voltage plateau at ~0.8 V *vs* Li^+/Li^0 due to the reduction of Fe^{3+} and Fe^{2+} to Fe^0 in the conversion reaction $Fe_3O_4 + 8e^- + 8Li^+ \rightarrow Fe^0 + 4Li_2O$, followed by a

sloping curve down to the cutoff voltage of 0.005 V. A sloping plateau around 1.8 V in the first charge profile reflects the reverse reaction, which agrees well with the typical characteristic of voltage trends for Fe_3O_4 anode materials. It should be noted that no obvious plateau can be observed in the following charge and discharge cycles of Fe_3O_4@Fe_3C−C yolk−shell nanospindles, indicating the introduction of a carbon shell can reduce the polarization and thus benefit the efficiency of LIBs. The first Coulombic efficiency of Fe_3O_4@Fe_3C−C yolk−shell nanospindles is 68.3% of the initial capacity of 1091 mAh/g, which is attributed to the formation of the solid electrolyte interface (SEI) layer on their surface,[7,15,37,38] as seen also from the shape difference between the discharge voltage profiles of the first and second cycle. In the second and third cycles, the Columbic efficiencies dramatically increase to 88% and 92.3%, indicating the rapid stabilization of the SEI layer.

In order to test the ultrafast charging and discharging capability of the electrodes, the cell capacities of the Fe_3O_4@Fe_3C−C yolk−shell nanospindles, Fe_3O_4@C core@shell nanospindle, and pure Fe_3O_4 NPs were evaluated at various current densities ranging from 500 to 10 000 mA/g, as shown in Figure 4b,c. The as-prepared Fe_3O_4@Fe_3C−C yolk−shell nanospindles show much higher capacity than Fe_3O_4@C core@shell nanospindles and pure Fe_3O_4 NPs under different current densities. The rate performance of Fe_3O_4@Fe_3C−C yolk−shell nanospindles was excellent. The capacities of Fe_3O_4@Fe_3C−C yolk−shell nanospindles are 530.2, 470.4, and 423.3 mAh/g at the 20th cycles of 1000, 1500, and 2000 mA/g, respectively, which are superior to those of the pure Fe_3O_4 (only 85 mAh/g at 1000 mA/g) and Fe_3O_4@C core@shell NPs (406 mAh/g for Fe_3O_4@C core@shell NPs at 1000 mA/g) under the same conditions. Most notably, the rate performance of Fe_3O_4@Fe_3C−C yolk−shell nanospindles is much better than those of the previously reported Fe_3O_4-based anode materials, such as an Fe_3O_4−C yolk−shell composite,[13] carbon nanotube@Fe_3O_4@C coaxial nanocables,[8] Fe_3O_4/porous carbon,[27,39] and Fe_3O_4/graphene composites[5,15,37,40] (Table S2).

The capacity performance of Fe/C-450 and Fe/C-650 obtained by carbonizing α-Fe_2O_3@RF at 450 and 650 °C was also tested under the same conditions (Figure S7). Both of them show a poor capacity due to the dominating Fe phase (proved by XRD data shown in Figure S5) in these two samples, which possesses a low theoretical capacity.[41]

The heterostructured Fe_3O_4@Fe_3C−C yolk−shell nanospindles also possess excellent cyclic capacity retention. Figure 4d shows the charge and discharge capacities and corresponding Coulombic efficiency as a function of cycle number at a constant current density of 500 mA g^{-1} following the test process of Figure 4c. The initial reversible capacity of the yolk−shell nanospindles is up to 809.2 mAh/g, which

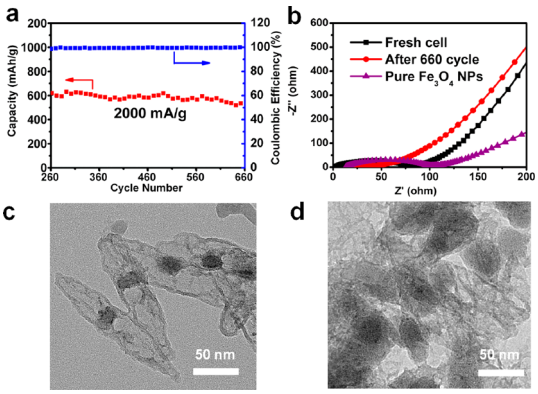

Figure 5. (a) Cycling performance of Fe_3O_4@Fe_3C−C yolk−shell nanospindles at 2000 mA g^{-1}, from the 260th to 660th cycle. (b) EIS of Fe_3O_4@Fe_3C−C yolk−shell nanospindles before and after cycling and pure Fe_3O_4 NPs. (c, d) TEM images of Fe_3O_4@Fe_3C−C yolk−shell nanospindles (c) and Fe_3O_4@C core@shell nanospindles (d) after the 660th cycle.

gradually reaches a maximum value of 1128.3 mAh g^{-1} and then shows almost no capacity fading for the subsequent 100 cycles (1120.2 mAh/g at the 560th cycle, a retention of 99.2%) with a nearly 100% Coulombic efficiency. It is worthy of noting that this increasing phenomenon has also been demonstrated in recent studies for a metal oxide electrode in long-term cycling for LIBs.[4,8,15,37] In our case, two main possibilities are given as follows. (i) The interface effect of Fe_3O_4/Fe_3C provides more active sites for additional Li^+ storage (Figure 4e).[4,15,18] (ii) The increment of capacity in the initial stage occurred with irreversible generation of Fe NPs,[42] which can increase the overall conductivity of the electrode (in accordance with the impedance result below, Figure 5b).[15] As a comparison, the Fe_3O_4@C core@shell nanospindles show an inferior cycle stability with a reversible capacity of only 365.4 mAh/g at the 560th cycle, which is 64.8% of the initial reversible capacity (563.2 mA h/g). For pure Fe_3O_4 NPs, without the carbon and Fe_3C shells, the capacity dramatically dropped from 1030.3 mA h/g (the first cycle) to 281.4 mA h g^{-1} at the tenth cycle and finally reached 122.2 mA h/g at the 355th cycle (11.9% of the initial reversible capacity). Long-term cycles of Fe_3O_4@Fe_3C−C yolk−shell nanospindles at a very high current density of 2000 mA h/g are subsequently shown in Figure 5a. After an additional 400 cycles, a reversible capacity of as high as 539.7 mA h/g can still be maintained (a retention of 86.4%), and we further compared the LIB performance of our Fe_3O_4@Fe_3C−C yolk−shell nanospindles with various reported Fe_3O_4-based anodes (Table S2). Obviously, Fe_3O_4@Fe_3C−C yolk−shell nanospindles exhibit overwhelming rate performance and cycling life.

The above comparison results confirm the crucial roles of both sufficient internal void space and the Fe_3C shell and carbon cage of Fe_3O_4@Fe_3C−C yolk−shell nanospindles on enhancing LIB capacity, rate capability, and stability. (a) The porous spindle-like carbon shell

plays an important role in enhancing the electrical conductivity and mass transportation, reducing the electrode pulverization during discharge/charge at high current densities. This has been proved by the electrochemical impedance spectra (EIS) of the Fe_3O_4@Fe_3C–C yolk–shell nanospindles and the pure Fe_3O_4 NPs before and after the stability test (Figure 5b). The Fe_3O_4@Fe_3C–C yolk–shell nanospindles have a lower resistance (~77.0 Ω) than the pure Fe_3O_4 NPs (~87.8 Ω). After 660 cycles, the resistance of the Fe_3O_4@Fe_3C–C yolk–shell nanospindles reaches 26.8 Ω, much smaller than that before cycling. This may be attributed to the sufficient wetting of electrolyte in the porous battery electrodes and the charged Li^+ intercalation.[8] (b) A possible interfacial lithium ion storage effect in the oxide/carbide heterogeneous structure is responsible for the improved performance of Fe_3O_4@Fe_3C–C yolk–shell nanospindles (Figure 4e).[17,18] (c) The self-formed yolk–shell spindle-shaped structure with enough space and good mechanical stability can effectively buffer the internal stress induced by volume variation of electrode materials during cycling. This was further confirmed by comparing the TEM images of the Fe_3O_4@Fe_3C–C yolk–shell nanospindles (Figure 5c) and Fe_3O_4@C core@shell nanospindles (Figure 5d) after the cycling test. We can see that the core NPs expand to some degree, but no pulverization and aggregation are observed even after 660 cycles in the Fe_3O_4@Fe_3C–C yolk–shell nanospindles. Moreover, the yolk–shell structural integrity can be well preserved even at the harsh charge/discharge cycles at 2000 mA g^{-1}. However, under identical conditions, Fe_3O_4@C core@shell nanospindles show a large change in their morphology (Figure 5d).

CONCLUSIONS

To summarize, we have designed and synthesized novel Fe_3O_4@Fe_3C–C yolk–shell nanospindles through *in situ* thermally annealing the as-made Fe_2O_3@RF core@shell nanospindles at high temperature (550 °C). In such a structure, a heterogeneous Fe_3O_4@Fe_3C core@shell NP (15–25 nm) is sandwiched in the compartment of a hollow carbon nanospindle (30 nm in width and 100 nm in length). An initial study on the formation mechanism of Fe_3O_4@Fe_3C–C yolk–shell nanospindles was carried out through changing the annealing temperature and carbon precursor. The control experiments reveal that (i) both the proper annealing temperature and RF carbon precursor are the key to the *in situ* formation of well-defined Fe_3O_4@Fe_3C–C yolk–shell nanospindles; (ii) the RF resin-based carbon shell exhibits a larger pore size and volume than the glucose-based carbon shell, providing a better pathway for the Fe getting out, leading to our peculiar yolk–shell structure.

Such intriguing yolk–shell architectures with very sufficient internal void space make them work as a new class of anode materials for developing LIBs with high capacity and rate capability as well as high stability. They can provide a dual role in boosting the performance of LIBs. The very sufficient internal void space provided by Fe_3O_4@Fe_3C–C yolk–shell nanospindles, which is different from previous yolk–shell structures with small internal void space, can provide a much larger space for the expansion and contraction of Fe_3O_4@Fe_3C NPs during the lithiation/dethiation process, and the Fe_3C shell on Fe_3O_4 NPs is effective in minimizing the dissolution and fracture of Fe_3O_4 core. We found that compared to the Fe_3O_4 NPs (122.2 mAh g^{-1}) and Fe_3O_4@C core@shell nanospindles (365.4 mAh g^{-1}), the as-obtained Fe_3O_4@Fe_3C–C yolk–shell nanospindles show a much higher stable specific capacity of 1128.3 mAh g^{-1} at 500 mA g^{-1}, excellent rate capability (604.8 mAh g^{-1} at 2000 mA g^{-1}), and excellent cycling stability. We expect that the strategy developed in this study may open a new way to prepare other transition-metal-based yolk–shell nanostructures with sufficient internal void space for next-generation LIBs.

EXPERIMENTAL SECTION

Synthesis of Fe_3O_4@Fe_3C–C Yolk–Shell Nanospindles. For a typical procedure, α-Fe_2O_3 nanospindles were prepared by aging a solution of 0.02 M $FeCl_3$ and NaH_2PO_4 at 105 °C for 48 h.[22] Then, 14.4 mg of α-Fe_2O_3 nanospindles was dispersed by ultrasonication in an ethanol/water mixture with a volume ratio of 1:1, followed by the addition of 10 μL of ammonia (28%). After further ultrasonication for 10 min, 10 mg of resorcinol and 14 μL of formaldehyde were sequentially added into the above mixture, followed by sonicating for 30 min. The suspension was transferred to a Teflon-lined stainless-steel autoclave and heated at 100 °C in an electric oven for 24 h. The resulting product was harvested by centrifugation, washed with water and ethanol, and dried at 50 °C overnight. Afterward, the as-prepared α-Fe_2O_3@RF core/shell nanospindles were annealed at 550 °C for 4 h with a heating rate of 1 °C/min under a N_2 atmosphere. Subsequently, the carbonized product was ultrasonically dispersed in 20 mL of ethanol. After aging for 2 h, the Fe_3O_4@Fe_3C–C yolk–shell nanospindles were obtained from the upper black "ink" by centrifugation and drying.

Synthesis of Fe_3O_4@C Core/Shell Nanospindles. The Fe_3O_4@C core@shell nanospindles were synthesized according to a modified carbon thermal method.[3] In a typical synthesis, 0.3 g of α-Fe_2O_3 nanospindles was dispersed in 5 mL of water by ultrasonication to form a suspension. Then 1.5 g of D-glucose monohydrate ($C_6H_{12}O_6 \cdot H_2O$) was dissolved in another 40 mL of DI water and added to the former suspension with another 20 mL of ethanol under ultrasonication. The resulting suspension was transferred to a 100 mL Teflon-lined stainless-steel autoclave, which was then heated at 190 °C in an electric oven for 12 h. The carbon precursor-coated hematite particles were harvested by centrifugation, washed with water, and then dried at 50 °C overnight. The resulting sample was annealed at 550 °C for 4 h at a heating rate of 1 °C min^{-1} under a N_2 atmosphere before it was allowed to cool to room temperature.

Synthesis of Fe_3O_4 NPs. The preparation of Fe_3O_4 NPs was carried out in a well-established chemical co-precipitation method.[35,36]

Typically, 4.73 g of $FeCl_3 \cdot 6H_2O$ and 1.99 g of $FeCl_2 \cdot 4H_2O$ were dissolved in 55 mL of deoxygenated water at 57 °C under N_2 protection. Subsequently, 5 mL of ammonium hydroxide was quickly injected into the above Fe^{2+}/Fe^{3+} salt solution, resulting in the formation of the black precipitate of magnetic NPs. After 15 min, 2 mL of ammonium hydroxide was additionally added to the above reaction system. The reaction was maintained at 57 °C for another 2 h, and the mixture was then cooled to room temperature. The resulting black precipitate was washed with deionized water several times and dried under vacuum.

Characterization. SEM and TEM images were taken using an FE-SEM (JEOR JSM-6700F, accelerating voltage of 5 kV) and an FEI Tecnai G2 20 (accelerating voltage of 200 kV), respectively. Elemental analysis was performed using energy-dispersive X-ray spectroscopy and electron energy loss spectroscopy equipped in the TEM. X-ray diffraction patterns were obtained on a Rigaku D/MAX-3B using Cu Kα radiation (λ = 1.5406 Å). TGA was carried out using a Mettler Toledo TGA/DSC 1 analyzer at a heating rate of 5 °C min^{-1} under an air atmosphere. The Raman spectrum was recorded at ambient temperature with a Renishaw Microscope System RM2000 Raman spectrometer. The N_2 adsorption/desorption curve was determined by BET measurements using a Micromeritics ASAP 2020 surface area analyzer. XPS experiments were performed with an ESCA LAB 250 spectrometer using a focused monochromatic Al Kα ($h\nu$ = 1486.6 eV) X-ray beam with a diameter of 200 μm.

Electrochemical Measurements. Electrochemical measurements were performed using coin-type 2032 cells. The working electrodes were prepared by mixing active materials, carbon black, and poly(vinyl difluoride) in 1-methyl-2-pyrrolidinone at a weight ratio of 80:10:10 and pasted on pure copper foil. The electrolyte consists of a solution of 1 M $LiPF_6$ in ethylene carbonate/dimethyl carbonate/diethyl carbonate (volume ratio of 1:1:1). Pure lithium foil was used as counter electrode, and the separator was a polypropylene membrane from Celgard. The cells were assembled in an argon-filled glovebox with the concentrations of moisture and oxygen below 1 ppm. The charge and discharge performances were carried out on an Arbin Instruments test system within a range of 0.005−3 V at different current densities. Electrochemical impedance spectral measurements were carried out in the frequency range from 100 kHz to 0.01 Hz on a CHI 660D electrochemical workstation.

Conflict of Interest: The authors declare no competing financial interest.

Acknowledgment. This work was financially supported by the National Natural Science Foundation of China (Nos. 21101141 and 51173170), the Program for New Century Excellent Talents in Universities (NCET), a J. Robert Oppenheimer Distinguished Fellowship, and the Open Project Foundation of Key Laboratory of Advanced Energy Materials Chemistry of Nankai University (2015-32).

Supporting Information Available: Additional SEM, TEM, TGA, XRD, BET, and electrochemical characterizations and additional tables. This material is available free of charge *via* the Internet at http://pubs.acs.org.

REFERENCES AND NOTES

1. Poizot, P.; Laruelle, S.; Grugeon, S.; Dupont, L.; Tarascon, J.-M. Nano-Sized Transition-Metal Oxides as Negative-Electrode Materials for Lithium-Ion Batteries. *Nature* **2000**, *407*, 496–499.
2. Taberna, P. L.; Mitra, S.; Poizot, P.; Simon, P.; Tarascon, J.-M. High Rate Capabilityies Fe_3O_4-Based Cu Nano-Architectured Electrodes for Lithium-Ion Battery Applications. *Nat. Mater.* **2006**, *5*, 567–573.
3. Zhang, W.-M.; Wu, X.-L.; Hu, J.-S.; Guo, Y.-G.; Wan, L.-J. Carbon Coated Fe_3O_4 Nanospindles as a Superior Anode Material for Lithium-Ion Batteries. *Adv. Funct. Mater.* **2008**, *18*, 3941–3946.
4. He, C. N.; Wu, S.; Zhao, N. Q.; Shi, C. S.; Liu, E. Z.; Li, J. J. Carbon-Encapsulated Fe_3O_4 Nanoparticles as a High-Rate Lithium Ion Battery Anode Material. *ACS Nano* **2013**, *7*, 4459–4469.
5. Lei, C.; Han, F.; Sun, Q.; Li, W. C.; Lu, A. H. Confined Nanospace Pyrolysis for the Fabrication of Coaxial Fe_3O_4@C Hollow Particles with a Penetrated Mesochannel as a Superior Anode for Li-Ion Batteries. *Chem.—Eur. J.* **2014**, *20*, 139–145.
6. Wang, L.; Liang, J.; Zhu, Y.; Mei, T.; Zhang, X.; Yang, Q.; Qian, Y. Synthesis of Fe_3O_4@C Core-Shell Nanorings and Their Enhanced Electrochemical Performance for Lithium-Ion Batteries. *Nanoscale* **2013**, *5*, 3627–3631.
7. Kang, E.; Jung, Y. S.; Cavanagh, A. S.; Kim, G.-H.; George, S. M.; Dillon, A. C.; Kim, J. K.; Lee, J. Fe_3O_4 Nanoparticles Confined in Mesocellular Carbon Foam for High Performance Anode Materials for Lithium-Ion Batteries. *Adv. Funct. Mater.* **2011**, *21*, 2430–2438.
8. Cheng, J. L.; Wang, B.; Park, C.-M.; Wu, Y. P.; Huang, H.; Nie, F. D. CNT@Fe_3O_4@C Coaxial Nanocables: One-Pot, Additive-Free Synthesis and Remarkable Lithium Storage Behavior. *Chem.—Eur. J.* **2013**, *19*, 9866–9874.
9. Chen, Y.; Song, B. H.; Lu, L.; Xue, J. M. Ultra-Small Fe_3O_4 Nanoparticle Decorated Graphene Nanosheets with Superior Cyclic Performance and Rate Capability. *Nanoscale* **2013**, *5*, 6797–6803.
10. Ji, L.; Tan, Z.; Kuykendall, T. R.; Aloni, S.; Xun, S.; Lin, E.; Battaglia, V.; Zhang, Y. Fe_3O_4 Nanoparticle-Integrated Graphene Sheets for High-Performance Half and Full Lithium Ion Cells. *Phys. Chem. Chem. Phys.* **2011**, *13*, 7170–7177.
11. Chen, Y.; Song, B. H.; Tang, X. S.; Lu, L.; Xue, J. M. One-Step Synthesis of Hollow Porous Fe_3O_4 Beads−Reduced Graphene Oxide Composites with Superior Battery. *J. Mater. Chem.* **2012**, *22*, 17656–17662.
12. Hahn, B. P.; Long, J. W.; Mansour, A. N.; Pettigrew, K. A.; Osofsky, M. S.; Rolison, D. R. Electrochemical Li-Ion Strorage in Defect Spinel Iron Oxides: the Critical Role of Cation Vacancies. *Energy Environ. Sci.* **2011**, *4*, 1495–1502.
13. Zhao, Y.; Li, J.; Wu, C.; Ding, Y.; Guan, L. A Yolk-Shell Fe_3O_4@C Composite as an Anode Material for High-Rate Lithium Batteries. *ChemPlusChem* **2012**, *77*, 748–751.
14. Zhang, H.; Zhou, L.; Noonan, O.; Martin, D. J.; Whittaker, A. K.; Yu, C. Tailoring the Void Size of Iron Oxide@Carbon Yolk-Shell Structure for Optimized Lithium Storage. *Adv. Funct. Mater.* **2014**, *24*, 4337–4342.
15. Luo, J.; Liu, J.; Zeng, Z.; Ng, C. F.; Ma, L.; Zhang, H.; Lin, J.; Shen, Z.; Fan, H. J. Three-Dimensional Graphene Foam Supported Fe_3O_4 Lithium Battery Anodes with Long Cycle Life and High Rate Cpability. *Nano Lett.* **2013**, *13*, 6136–6143.
16. Giordano, C.; Kraupner, A.; Fleischer, I.; Henrich, C.; Klingelhöfer, G.; Antonietti, M. Non-Conventional Fe_3C-Based Nanostructures. *J. Mater. Chem.* **2011**, *21*, 16963–16968.
17. Li, J.; Zou, M.; Chen, L.; Huang, Z.; Guan, L. An Efficient Bifunctional Catalyst of Fe/Fe_3C Carbon Nanofibers for Rechargeable Li-O_2 Batteries. *J. Mater. Chem. A* **2014**, *2*, 10634–10638.
18. Yang, Y.; Fan, X.; Casillas, G.; Peng, Z.; Ruan, G.; Wang, G.; Yacaman, M. J.; Tour, J. M. Three-Dimensional Nanoporous Fe_2O_3/Fe_3C−Graphene Heterogeneous Thin Films for Lithium-Ion Batteries. *ACS Nano* **2014**, *8*, 3939–3946.
19. Xiao, Y.; Sun, P. P.; Cao, M. H. Core-Shell Bimetallic Carbide Nanoparticles Confined in a Three-Dimentional N-Doped Carbon Conductive Network for Efficient Lithium Storage. *ACS Nano* **2014**, *8*, 7846–7857.
20. Lee, J.-S.; Park, G. S.; Kim, S. T.; Liu, M. L.; Cho, J. A Highly Efficient Electrocatalyst for the Oxygen Reduction Reaction: N-Doped Ketjenblack Incorporated into Fe/Fe_3C-Functionalized Melamine Foam. *Angew. Chem., Int. Ed.* **2013**, *52*, 1026–1030.
21. Wen, Z.; Ci, S.; Zhang, F.; Feng, X.; Cui, S.; Mao, S.; Luo, S.; He, Z.; Chen, J. Nitrogen-Enriched Core-Shell Structured Fe/Fe_3C-C Nanorods as Advanced Electrocatalysts for Oxygen Reduction Reaction. *Adv. Mater.* **2012**, *24*, 1399–1404.
22. Ozaki, M.; Kratohvil, S.; Matijevic, E. Formation of Monodispersed Spindle-Type Hematite Particles. *J. Colloid Interface Sci.* **1984**, *102*, 146–151.

23. Chen, Y.; Chen, H.; Zeng, D.; Tian, Y.; Chen, F.; Feng, J.; Shi, J. Core/Shell Structured Hollow Mesoporous Nanocapsules: A Potential Platform for Simultaneous Cell Imaging and Anticancer Drug Delivery. *ACS Nano* **2010**, *4*, 6001–6013.
24. Lou, X. W.; Yuan, C.; Archer, L. A. Double-Walled SnO_2 Nano-Cocoons with Movable Magnetic Cores. *Adv. Mater.* **2007**, *19*, 3328–3332.
25. Yang, S. B.; Sun, Y.; Chen, L.; Hernandez, Y.; Feng, X. L.; Müllen, K. Porous Iron Oxide Ribbons Grown on Graphene for High-Performance Lithium Storage. *Sci. Rep.* **2012**, *2*, 427–433.
26. Ban, C. M.; Wu, Z. C.; Gillaspie, D. T.; Chen, L.; Yan, Y. F.; Blackbum, J. L.; Dillon, A. C. Nanostructured Fe_3O_4/SWNT Electrode: Binder-Free and High Rate Li-Ion Anode. *Adv. Mater.* **2010**, *22*, E145–E149.
27. Liao, Y.; Pan, K.; Wang, L.; Pan, Q.; Zhou, W.; Miao, X.; Jiang, B.; Tian, C.; Tian, G.; Wang, G.; *et al*. Facile Synthesis of High-Crystallinity Graphitic Carbon/Fe_3C Nanocomposites as Counter Electrodes for High-Efficiency Dye-Sensitized Solar Cells. *ACS Appl. Mater. Interfaces* **2013**, *5*, 3663–3670.
28. Geng, J. F.; Jefferson, D. A.; Johnson, F. G. Direct Conversion of Iron Stearate into Magnetic Fe and Fe_3C Nanocrystals Encapsulated in Polyhedral Graphite Cages. *Chem. Commun.* **2004**, 2442–2443.
29. Fujii, T.; de Groot, F. M. F.; Sawatzky, G. A.; Voogt, F. C.; Hibma, T.; Okada, K. *In Situ* XPS Analysis of Various Iron Oxide Films Grown by NO_2-Assisted Molecular-Beam Epitaxy. *Phys. Rev. B* **1999**, *59*, 3195–3202.
30. Chen, L.-F.; Zhang, X.-D.; Liang, H.-W.; Kong, M. G.; Guan, Q.-F.; Chen, P.; Wu, Z.-F.; Yu, S.-H. Synthesis of Nitrogen-Doped Porous Carbon Nanofibers as an Efficient Electrode Material for Supercapacitors. *ACS Nano* **2012**, *6*, 7092–7102.
31. Yang, Z. C.; Shen, J. G.; Aecher, L. A. An *in Situ* Method of Application as Anode Materials for Lithium-Ion Batteries. *J. Mater. Chem.* **2011**, *21*, 11092–11097.
32. Wang, S. P.; Zhang, J. N.; Shang, P.; Li, Y. Y.; Chen, Z. M.; Xu, Q. N-Doped Carbon Spheres with Herarchical Micropore-Nanosheet Networks for High Performance Supercapacitors. *Chem. Commun.* **2014**, *50*, 12091–12094.
33. Jiang, H.; Hu, Y.; Guo, S.; Yan, C.; Lee, P. S.; Li, C. Rational Design of MnO/Carbon Nanopeapods with Internal Void Space for High-Rate and Long-Life Li-Ion Batteries. *ACS Nano* **2014**, *8*, 6038–6046.
34. Zhang, J. N.; Guo, S. J.; Wei, J. Y.; Xu, Q.; Yan, W. F.; Fu, J. W.; Wang, S. P.; Cao, M. J.; Chen, Z. M. High-Efficiency Encapsulation of Pt Nanoparticles into the Channel of Carbon Nanotubes as an Enhanced Electrocatalyst for Methanol Oxidation. *Chem.—Eur. J.* **2013**, *19*, 16087–16092.
35. Wang, X.; Wang, M.; Fu, J.; Zhang, C.; Xu, Q. Facile Fabrication of Core−Shell Structured Magnetic Fe_3O_4/Cross-Linked Polyphosphazene Nanocomposite Particles with High Stability. *J. Nanopart. Res.* **2013**, *15*, 1853–1852.
36. Behera, S. K. Enhanced Rate Performance and Cyclic Stability of Fe_3O_4-Graphene Nanocomposites for Li Ion Battery Anodes. *Chem. Commun.* **2011**, 10371–10373.
37. Chen, Y.; Song, B.; Li, M.; Lu, L.; Xue, J. Fe_3O_4 Nanoparticles Embedded in Uniform Mesoporous Carbon Spheres for Superior High-Rate Battery Applications. *Adv. Funct. Mater.* **2014**, *24*, 319–326.
38. Zhu, X.; Zhu, Y.; Murali, S.; Stoller, M. D.; Ruoff, R. S. Nanostructured Reduced Graphene Oxide/Fe_2O_3 Composite as a High-Performance Anode Material for Lithium Ion Batteries. *ACS Nano* **2011**, *5*, 3333–3338.
39. Chen, G.; Zhou, M.; Catanach, J.; Liaw, T.; Fei, L.; Deng, S.; Luo, H. Solvothermal Route Based *in Situ* Carbonization to Fe_3O_4@C as Anode Material for Lithium Ion Battery. *Nano Energy* **2014**, *8*, 126–132.
40. Li, X. Y.; Huang, X. L.; Liu, D. P.; Wang, X.; Song, S. Y.; Zhou, L.; Zhang, H. J. Synthesis of 3D Hierarchical Fe_3O_4/Graphene Composites with High Lithium Storage Capacity and for Controlled Drug Delivery. *J. Phys. Chem. C* **2011**, *115*, 21567–21573.
41. Su, L. W.; Zhong, Y. R.; Zhou, Z. Role of Transition Metal Nanoparticles in the Extra Lithium Storage Capacity of Transition Metal Oxides: A Case Study of Hierarchical Core-Shell Fe_3O_4@C and Fe@C Microspheres. *J. Mater. Chem. A* **2013**, *1*, 15158–15166.
42. Huang, X.; Chen, J.; Lu, Z.; Yu, H.; Yan, Q.; Hng, H. H. Carbon Inverse Opal Entrapped with Electrode Active Nanoparticles as High-Performance Anode for Lithium-Ion Batteries. *Sci. Rep.* **2013**, *3*, 2317–2325.